ADVANCED FUNCTIONAL MATERIALS
www.afm-journal.de

Effective Eradication of Tumors by Enhancing Photoacoustic-Imaging-Guided Combined Photothermal Therapy and Ultrasonic Therapy

Caina Xu, Yanbing Wang, Erlei Wang, Nan Yan, Shu Sheng, Jie Chen, Lin Lin, Zhaopie Guo, Huayu Tian, and Xuesi Chen*

Exploiting a comprehensive strategy that processes diagnosis and therapeutic functions is desired for eradicating tumors. In this study, two versatile nanoparticles are introduced: one is polyethylene glycol- and polyethyleneimine-modified gold nanorods (mPEG–PEI–AuNRs), and the other is formed by electrostatic interactions between mPEG–PEI and calcium carbonate nanoparticles (mPEG–PEI/CaNPs). These two nanoparticles possess following favorable properties: 1) mPEG–PEI–AuNRs and mPEG–PEI/CaNPs show not only high cell uptake in acidic tumoral pH, but also efficient accumulation in tumors with prolonged circulation. 2) mPEG–PEI/CaNPs can generate carbon dioxide (CO_2) bubbles in acidic tumoral environment and the photoacoustic (PA) signals from mPEG–PEI–AuNRs can be enhanced with the generation of CO_2 bubbles. 3) The tumors can be eradicated by combining photothermal therapy (PTT) with ultrasonic therapy (UST) under the near-infrared (NIR) laser and ultrasonic irradiation with the presence of mPEG–PEI–AuNRs and CO_2 bubbles from mPEG–PEI/CaNPs. The detailed evaluation of cellular uptake, photothermal property of mPEG–PEI–AuNRs, CO_2 bubbles' generation from mPEG–PEI/CaNPs, imaging, and combined PTT and UST are carried out in vitro or in vivo. This work has great potential usage for diagnosis and treatment in the future.

1. Introduction

Photoacoustic imaging (PAI), which has emerged as a noninvasive imaging technique, can combine the spectral selectivity of optical absorption with the high resolution and depth penetration of ultrasonic imaging.[1] Because of the conversion from optical absorption to ultrasonic (US) energy, PAI can be used to image deep tissues with high resolution.[2] PAI has also been proven to track the drug delivery, drug uptake, and accumulation in tumors in vivo.[3] As the optical absorption of endogenous chromophores (e.g., hemoglobin), PAI has been used to be an effective method for imaging blood vessels. Nevertheless, due to the low absorption properties of endogenous chromophores, PA signals are relatively weak, limiting the application of endogenous contrast in PAI.[4] In addition, exogenous contrasts have been developed as contrast agents for visualizing tissue structures and functions.[5] However, the PA signals may be limited by thermal expansion with low-efficient mechanisms of light–sound energy conversion and relatively low acoustic waves.[6] Therefore, it is highly desirable to explore exogenous contrast agents for PAI enhancement.

Microbubbles, as the sensitive and biocompatible contrast agents, have been used in diagnostic ultrasonic imaging.[7] Microbubbles have, already, widely been used in clinic due to their highly scattering acoustic properties.[8] In addition, bubbles could also be used as therapeutic agents for ultrasonic treatment.[6,8] Bubbles could instantly explode by ultrasonic irradiation, thus induce the necrosis of tumor cells and inhibit the growth of tumors.[9] However, the inherent drawbacks of bubbles especially for water-soluble free gas bubbles, e.g., carbon dioxide (CO_2) bubbles have limited their application in vivo, as these bubbles have short half-life in blood circulation due to the rapid gas diffusion and biological clearance.[10] Lee's group developed bubble-generating mineralized nanoparticles for ultrasonic imaging.[11] These bubble-generating mineralized nanoparticles could generate CO_2 bubbles at tumoral acid pH and showed strong echogenic signals for ultrasonic imaging. Therefore, the enhancing contract agent based on bubbles generated in response to acidic tumoral environment would be highlighted the need for monitoring the tumors' accumulation and guiding precise therapy.

On the other hand, combination of more than one therapeutic strategy with different mechanism is evolved

Prof. C. Xu, Dr. Y. Wang, Dr. N. Yan, S. Sheng, Prof. J. Chen, L. Lin, Prof. Z. Guo, Prof. H. Tian, Prof. X. Chen
Key Laboratory of Polymer Ecomaterials
Changchun Institute of Applied Chemistry
Chinese Academy of Sciences
Changchun 130022, P. R. China
E-mail: thy@ciac.ac.cn
Prof. E. Wang
College Food Science and Engineering
Jilin University
Changchun 130062, P. R. China
The ORCID identification number(s) for the author(s) of this article can be found under https://doi.org/10.1002/adfm.202009314.

DOI: 10.1002/adfm.202009314

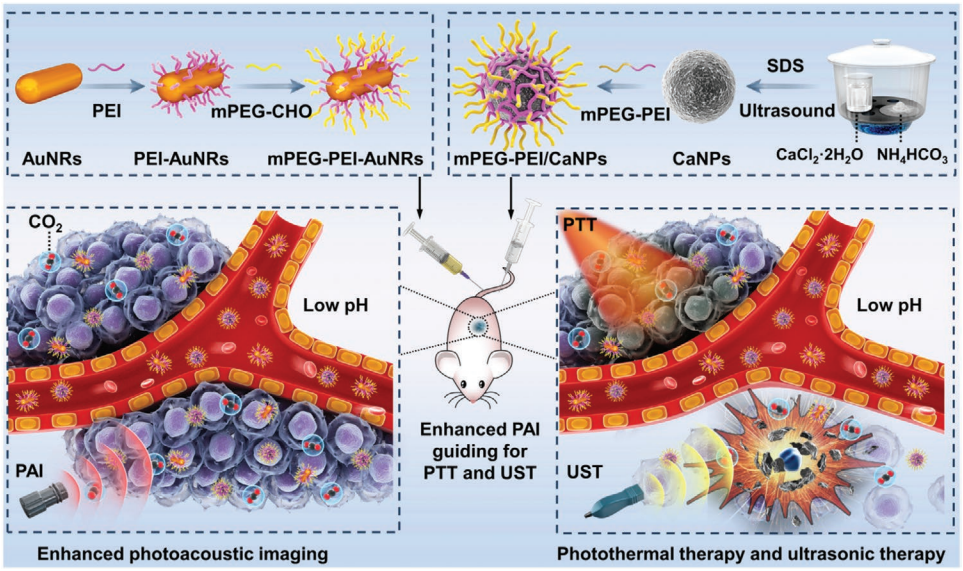

Scheme 1. Schematic illustration of designed mPEG–PEI–AuNRs and mPEG–PEI/CaNPs with enhancing photoacoustic imaging for combination of PTT and UST.

as a promising potential in cancer therapy.[12] Photothermal therapy (PTT) has been widely used to be a promising avenue for cancer treatment; the high temperature generated from photothermal agents under near-infrared (NIR) light irradiation could lead to ablate tumor cells.[13] PTT exhibits many advantageous features including low cost, minimally invasive approach, specific tumor treatment, and low collateral damage to the normal tissue.[3,13f,14] Nevertheless, as the intrinsic drawback of optical therapy, it is difficult to eradicate tumors by PTT alone, especially for the deep-located tumors. The reason is that the laser intensity would decline with the increasing depth.[3] However, ultrasonic therapy (UST) can treat deep-seated tumors with much larger penetration depth. Meanwhile, UST also has some other advantages, such as noninvasive treatment and universality for local therapy.[9,15] Therefore, combination of PTT and UST was highly desirable for eradicating tumors.

In this study, we have developed two kinds of nanoparticles, mPEG–PEI–AuNRs and mPEG–PEI/CaNPs, for PA contrast enhanced imaging and combining PTT and UST (**Scheme 1**). At first, they were labeled by Cyanine 5 (Cy5). mPEG–PEI–AuNRs and mPEG–PEI/CaNPs were injected via tail vein, and then the maximum accumulation time in tumor tissue was tracked. When mPEG–PEI–AuNRs and mPEG–PEI/CaNPs arrived at tumor tissue, the PA signals form mPEG–PEI–AuNRs were enhanced with the generation of CO_2 bubbles from mPEG–PEI/CaNPs; thus, they could monitor the tumors' accumulation and guide for precise therapy. On the other hand, the generated CO_2 bubbles could instantly explode by ultrasonic irradiation, thus, induce the necrosis of tumor cells and inhibit the growth of tumors. Furthermore, the tumors were eradicated by combining with PTT and UST under the NIR laser and ultrasonic irradiation. Therefore, the generated bubbles' strategy was introduced for enhancing PAI and UST, and this combining PTT with UST method is highly promising for the extensive applications of eradicating tumors.

2. Results and Discussion

2.1. Synthesis and Characterization of mPEG–PEI–AuNRs and mPEG–PEI/CaNPs

The AuNRs were synthesized using the seed-mediated growth method and thiolated PEI (PEI−SH) grafted on the surface of AuNRs via Au−S bond.[16] mPEG–PEI–AuNRs were prepared by aldehyde-modified polyethylene glycol (mPEG−CHO) via Schiff base reaction (**Figure 1**a).[17] The as-prepared PEI−SH was characterized by Fourier transform infrared (FTIR) spectra (Figure S1, Supporting Information), the transmission bands at 1655 and 1575 cm^{-1} could be attributed to the amide I and II bands, respectively.[18] Besides, a slight redshift of the localized surface plasmon resonance (LSPR) band in UV–vis–NIR spectra (Figure S2, Supporting Information) was observed in PEI–AuNRs, which could be due to the local refractive index change after PEI modification.[19] The aldehyde-group-modified PEG was synthesized according to the previous reported method,[17,20] and the mPEG−CHO was characterized by ^{1}H NMR (Figure S3, Supporting Information). The mPEG–PEI could be prepared to form Schiff base bonds between the aldehyde groups of mPEG−CHO and the amino groups of PEI, and the mPEG–PEI was characterized by ^{1}H NMR (Figure S3, Supporting Information). As this "click" reaction could happen on the surface of PEI–AuNRs, the mPEG–PEI–AuNRs were easily prepared via the Schiff base reaction.[20] The peak of aldehyde groups (at 10 ppm) completely disappeared at pH 7.4. However, the Schiff base bonds could rapidly cleave at the slightly acidic pH 6.8, and the aldehyde groups were restored in ^{1}H NMR spectrum, which indicated that PEG was detached from PEI. The morphology of AuNRs was measured by transmission electron microscopy (TEM), which showed that the aspect ratio of AuNRs was ≈3.7 (Figure 1b). And the AuNRs still retained their morphology, and there were no obvious changes after mPEG–PEI modification (Figure 1c). CaNPs were prepared

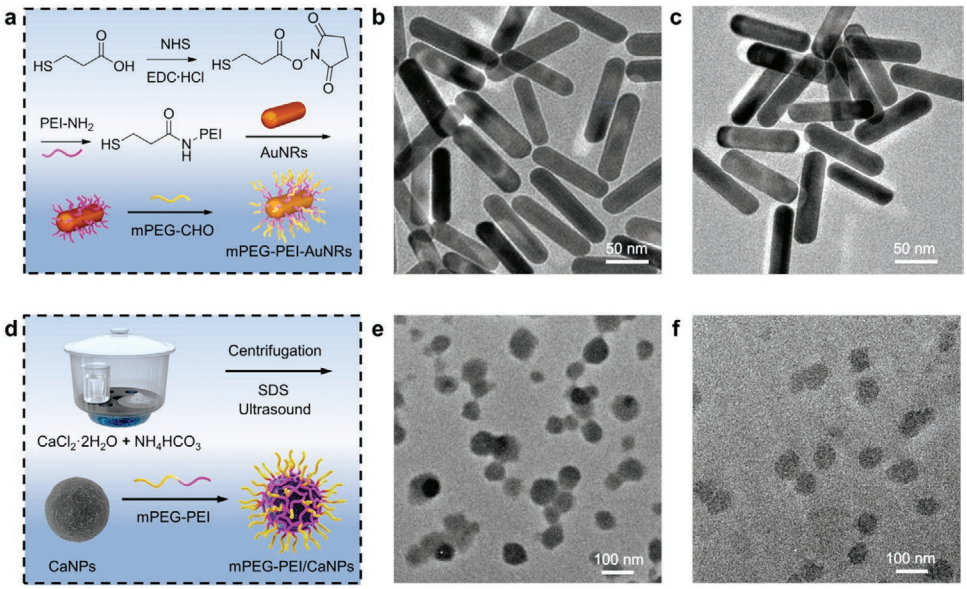

Figure 1. Preparation and characterization of mPEG–PEI–AuNRs and mPEG–PEI/CaNPs. a) Schematic illustration for the preparation and structure of mPEG–PEI–AuNRs. b,c) TEM images of the AuNRs, and mPEG–PEI–AuNRs, respectively (scale bar = 50 nm). d) Schematic illustration for the preparation and structure of mPEG–PEI/CaNPs. e,f) TEM images of the CaNPs and mPEG–PEI/CaNPs, respectively (scale bar = 100 nm).

using calcium chloride dihydrate ($CaCl_2 \cdot 2H_2O$) and ammonium bicarbonate (NH_4HCO_3) via vapor diffusion reaction in a desiccator (Figure 1d). mPEG–PEI/CaNPs were prepared via electrostatic interaction between the positive charge of mPEG–PEI and negative charge of CaNPs. The average diameter of CaNPs was ≈53 nm (Figure 1e). The morphology of mPEG–PEI/CaNPs showed good dispersion, which was attributed to the modification of mPEG–PEI (Figure 1f). Furthermore, the zeta potentials of mPEG–PEI–AuNRs and mPEG–PEI/CaNPs are shown in Figure S4 (Supporting Information). The zeta potential was sharply increased after PEI modification, which would be helpful for cell uptake. However, the zeta potential obviously decreased after PEG modification, which indicated that PEG effectively shielded the positive charges of PEI–AuNRs or PEI/CaNPs and would be beneficial for the long circulation. The above results suggested that mPEG–PEI–AuNRs and mPEG–PEI/CaNPs were successfully prepared through the Au—S bond, Schiff base reaction, and electrostatic interaction, respectively.

2.2. Cellular Uptake and Intracellular Distribution

The cellular uptake assay was evaluated by flow cytometry (FCM; Figure S5, Supporting Information). The cellular uptake of PEI–AuNRs or PEI/CaNPs was slightly affected at different incubation pH. In contrast, the cellular uptake of mPEG–PEI–AuNRs or mPEG–PEI/CaNPs at pH 6.5 was significantly higher than that at pH 7.4. The reason was due to the PEG detaching from mPEG–PEI–AuNRs or mPEG–PEI/CaNPs under acidic environment; the exposed higher positively charged PEI–AuNRs or PEI/CaNPs could interact with the negatively charged cell membranes and resulted in higher cellular uptake than that at pH 7.4. To further understand the localization of mPEG–PEI–AuNRs or mPEG–PEI/CaNPs, confocal laser scanning microscopy (CLSM) was employed to capture the treated MCF-7 cells (**Figure 2**). The results showed that the red fluorescence was significantly reduced after PEG modification, and the fluorescence from mPEG–PEI–AuNRs or mPEG–PEI/CaNPs exhibited obviously increased value under pH at 6.5 compared to that pH at 7.4, which was attributed to the removal of the PEG shielding in the acidic pH (Figure 2; Figure S6, Supporting Information). However, the fluorescence from PEI–AuNRs or PEI/CaNPs did not change significantly by varying the incubation pH. This result was consistent with the cell uptake assay and further confirmed that acidic pH could enhance the uptake efficiency.

2.3. Photothermal Property of mPEG–PEI–AuNRs and CO_2 Bubbles' Generation from mPEG–PEI/CaNPs

The photothermal performance of mPEG–PEI–AuNRs showed the concentration dependence (**Figure 3**a), in which the highest temperature reached 60 °C after an 808 nm NIR laser irradiation (0.8 W cm^{-2}) for 10 min at an Au concentration of 12.5 μg mL^{-1}, while that of pure water increased only 6 °C under the same conditions. mPEG–PEI–AuNRs exhibited excellent photostability after several cycles of NIR laser exposure (Figure 3b). Furthermore, mPEG–PEI–AuNRs showed high photothermal conversion efficiency (27.7 %), which is calculated according to the relation shown in Figure S7 (Supporting Information). The photothermal conversion efficiency of mPEG–PEI–AuNRs was higher than that of previously reported Au nanorods (21 %) and Au nanoshells (13 %).[21] Collectively, these results suggested that mPEG–PEI–AuNRs would be potential photothermal agents for PTT.

To verify CO_2 bubbles' generation from mPEG–PEI/CaNPs, the generation of CO_2 bubbles from mPEG–PEI/CaNPs was visualized using the optical microscopy. As shown in Figure S8

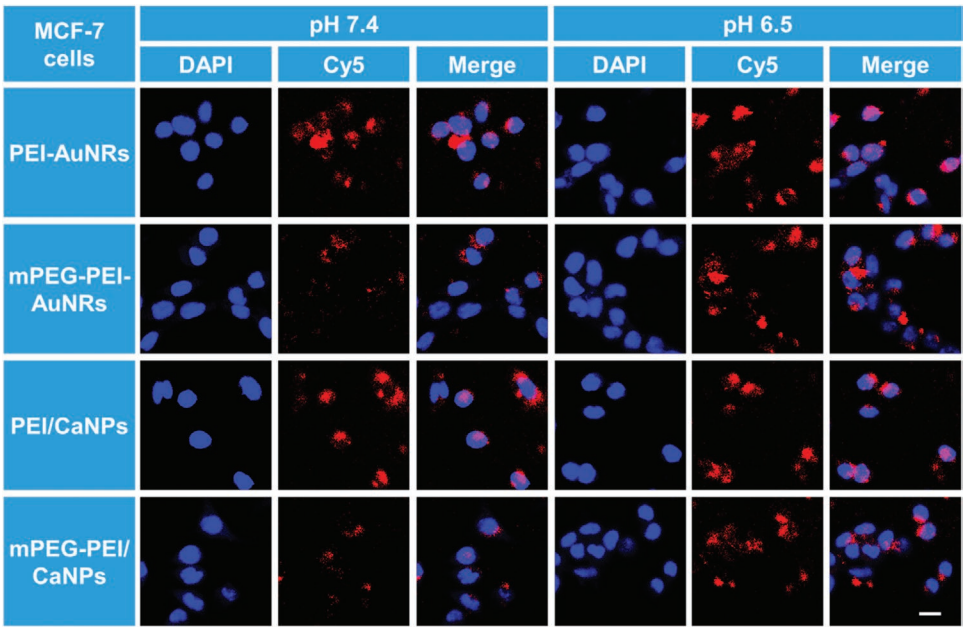

Figure 2. Cellular internalization of PEI–AuNRs, PEI/CaNPs, mPEG–PEI–AuNRs, and mPEG–PEI/CaNPs at pH 7.4 and 6.5 in MCF-7 cells. Blue and red represented DAPI (cell nuclei) and Cy5 fluorescence, respectively. Scale bar = 20 µm.

(Supporting Information), the CO_2 bubbles were generated at pH 6.5 after 60 min incubation. Interestingly, the bubbles generated from the mPEG–PEI/CaNPs gradually grew up with the incubation time increasing to 120 min. This phenomenon was likely due to the nanobubbles being into the microbubbles as the expansion or coalescence of CO_2 bubbles. However, there were a very few bubbles generated at pH 7.4 with the increasing time (data not shown). A gas chromatography mass spectrometer (GC–MS, AGILENT 5975) was employed to monitor the CO_2 generation rate of mPEG–PEI/CaNPs at pH 7.4, 6.5, and 5.0 (Figure S9, Supporting Information). About 40 mg of mPEG–PEI/CaNPs was placed in the sample bottle, and the sample bottle was vacuumed and replaced by nitrogen; 10 mL of phosphate-buffered solutions (PBS) at various pH (7.4, 6.5, and 5.0) was injected into the sample bottles. The results showed that the peak at 1.67 min represented CO_2 (Figure S9a, Supporting Information). And the CO_2 generation rates of mPEG–PEI/CaNPs at pH 6.5 and 5.0 conditions were significantly

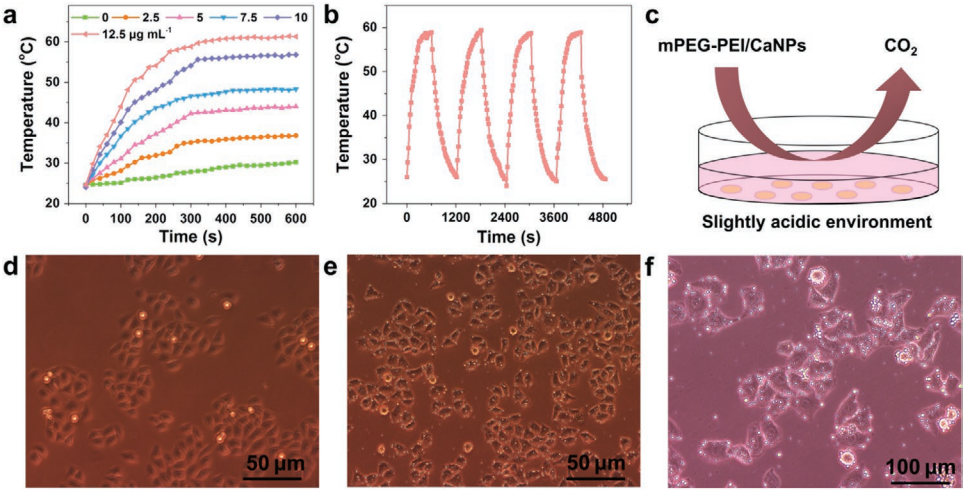

Figure 3. Photothermal property of mPEG–PEI–AuNRs and CO_2 bubbles' generation from mPEG–PEI/CaNPs. a) Temperature curves of different Au concentrations of mPEG–PEI–AuNRs (0, 2.5, 5, 7.5, 10, and 12.5 µg mL^{-1}) with an 808 nm laser irradiation (0.8 W cm^{-2}). b) Photostability of mPEG–PEI–AuNRs. The Au concentration of mPEG–PEI–AuNRs was 10 µg mL^{-1} with the laser power density of 0.8 W cm^{-2}. The 808 nm laser was turned on for 10 min and then turned off for each cycle. c) Scheme of the CO_2 bubbles' generation from mPEG–PEI/CaNPs at slightly acidic environment. The generation of CO_2 bubbles in HeLa cells d) without or e,f) with mPEG–PEI/CaNPs' incubation. The concentration of mPEG–PEI/CaNPs was 10 µg mL^{-1}, and the coincubated time with HeLa cells was 6 h. The Au and Ca contents were used to define the concentration of mPEG–PEI–AuNRs and mPEG–PEI/CaNPs in all experiments, respectively. The cells were observed by microscopy under d,e) (100 ×) and f) (200 ×) magnifications.

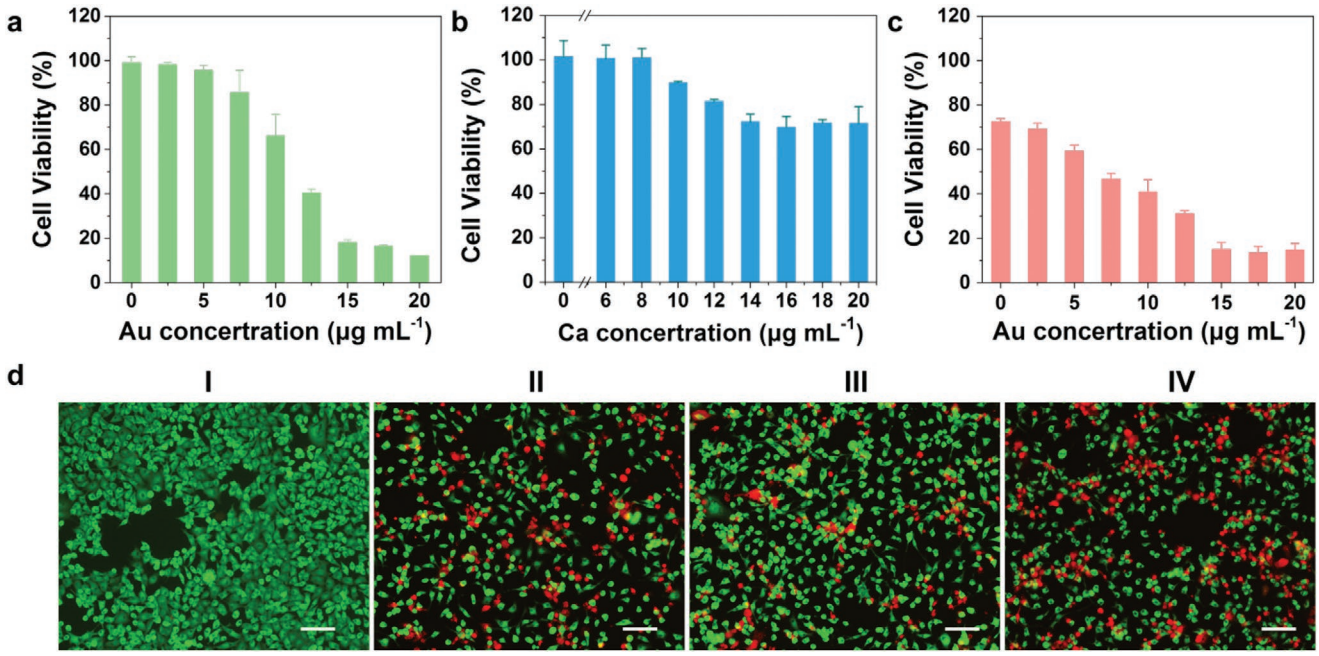

Figure 4. In vitro PTT and UST. a) Cell viability of MCF-7 cells treated with different concentrations of mPEG–PEI–AuNRs with 808 nm laser irradiation for 6 min. b) Cell viability of MCF-7 cells treated with different concentrations of mPEG–PEI/CaNPs with ultrasonic irradiation for 10 min (1 Hz, 1.5 W cm^{-2}). c) Cell viability of MCF-7 cells treated with different concentrations of mPEG–PEI–AuNRs and mPEG–PEI/CaNPs at 12 μg mL^{-1} under laser irradiation for 6 min and ultrasonic irradiation for 10 min (1 Hz, 1.5 W cm^{-2}). d) Fluorescence images of mPEG–PEI–AuNRs and mPEG–PEI/CaNPs coincubated MCF-7 cells stained with calcein AM (green, live cells) and PI (red, dead cells) under laser irradiation for 6 min and ultrasonic irradiation for 10 min (1 Hz, 1.5 W cm^{-2}). I: Control; II: mPEG–PEI–AuNRs (Au, 12.5 μg mL^{-1}); III: mPEG–PEI/CaNPs (Ca, 12 μg mL^{-1}); IV: mPEG–PEI–AuNRs and mPEG–PEI/CaNPs (Au, 12.5 μg mL^{-1}; Ca, 12 μg mL^{-1}). Scale bar = 100 μm. The Au and Ca contents were used to define the concentration of mPEG–PEI–AuNRs and mPEG–PEI/CaNPs in all experiments, respectively.

higher than that at pH 7.4 (Figure S9b, Supporting Information). The results illustrated that the rate of CO_2 generation was greatly affected by the pH value. In a slightly acidic tumor environment, the rate of CO_2 generation was faster, which was conducive to the generation of more bubbles in the tumor area, and which would be further beneficial for tumor treatment. To further confirm the CO_2 bubbles' generation from mPEG–PEI/CaNPs at slightly acidic environment, cells were incubated with mPEG–PEI/CaNPs at the concentration of 10 μg mL^{-1} for 6 h, then the cells were captured using optical microscopy (Figure 3c). Compared with cells without mPEG–PEI/CaNPs' incubation (Figure 3d), the obvious generation of CO_2 bubbles was observed in HeLa cells and MCF-7 cells with mPEG–PEI/CaNPs incubation (Figure 3e,f; Figure S10, Supporting Information). The results demonstrated that mPEG–PEI/CaNPs could generate CO_2 bubbles at acidic environment and might serve as theranostic agents for enhancing PAI and UST.

2.4. In Vitro Photothermal Therapy and Ultrasonic Therapy

Given that the photothermal property of mPEG–PEI–AuNRs and CO_2 bubbles' generation from mPEG–PEI/CaNPs, their corresponding activities against tumor cells were examined. The biocompatibilities of mPEG–PEI–AuNRs and mPEG–PEI/CaNPs were evaluated using 3-(4,5-dimethylthiazol-2-yl)-2,5-diphenyltetrazolium bromide (MTT) assay. The results showed that mPEG–PEI–AuNRs and mPEG–PEI/CaNPs did not exhibit any obvious toxic effects to MCF-7 cells (Figure S11, Supporting Information), HeLa cells (Figure S12, Supporting Information), and 293T cells (Figure S13, Supporting Information), which indicated that mPEG–PEI–AuNRs and mPEG–PEI/CaNPs had excellent biocompatibility. Next, the photothermal cytotoxicity of the mPEG–PEI–AuNRs was assessed in two tumor cell lines MCF-7 and HeLa cells (**Figure 4**a; Figure S14a, Supporting Information). The results exhibited a strong concentration-dependent cytotoxicity after NIR laser induced PTT with mPEG–PEI–AuNRs in cell lines. Furthermore, to evaluate the effect of ultrasonic therapy with mPEG–PEI/CaNPs, various concentrations of mPEG–PEI/CaNPs were added into MCF-7 or HeLa cells, and then the cells were exposed to ultrasonic irradiation (Figure 4b; Figure S14b, Supporting Information). The cell viability decreased when they were treated with different concentrations of mPEG–PEI/CaNPs by ultrasonic irradiation. The reason was attributed to the fact that mPEG–PEI/CaNPs could generate CO_2 bubbles at tumoral pH and explode to mechanically destroy by ultrasonic, which could consequently induce the necrotic cell death.[9,11] However, the cell viability changed a little after the concentration increased to 12 μg mL^{-1}, which indicated that the effects of UST were influenced lightly when the concentration is higher than the 12 μg mL^{-1}. Moreover, the combination of PTT and UST with mPEG–PEI–AuNRs and mPEG–PEI/CaNPs was determined in MCF-7 and HeLa cells. As expected, the results showed that the cell viability was much lower than that treated with laser irradiation or ultrasonic irradiation alone (Figure 4c; Figure S14c, Supporting Information). Meanwhile, MCF-7 or

HeLa cells treated with mPEG–PEI–AuNRs or mPEG–PEI/CaNPs were stained with calcein AM and propidium iodide (PI) after treatment, and the fluorescence images of calcein AM and PI co-stained cells also demonstrated the effectiveness of PTT and UST (Figure 4d; Figure S15, Supporting Information), which suggested that the combination with PTT and UST led to more effective cell death than that of PTT or UST alone. These results clearly revealed that the mPEG–PEI–AuNRs and mPEG–PEI/CaNPs could be effective PTT and UST agents.

2.5. In Vivo Imaging

To track the maximum accumulation time in tumor tissue, MCF-7 tumor-bearing Balb/c nude mice were divided into two groups: one was injected via tail vein with Cy5-labeled mPEG–PEI–AuNRs (Au, 200 μg mL^{-1}), the other was injected with Cy5-labeled mPEG–PEI/CaNPs (Ca, 100 μg mL^{-1}). The major organs and tumors were excised and imaged at different accumulation times. The results showed that both mPEG–PEI–AuNRs and mPEG–PEI/CaNPs reached maximum accumulation at 24 h post injection (Figure S16, Supporting Information). Moreover, the fluorescence of PEI–AuNRs and PEI/CaNPs could be visible with weak signals in tumors at 24 h post injection (Figure S17, Supporting Information). In contrast, mPEG–PEI–AuNRs and mPEG–PEI/CaNPs exhibited higher fluorescence intensities than that without PEG, which indicated that more effective accumulation in tumor tissue than that of PEI–AuNRs and PEI/CaNPs. The main reason was that PEG could effectively shield the positive charges of PEI and would be beneficial for the properties of stability and long circulation of PEI–AuNRs and PEI/CaNPs. At the same time, the heart, liver, spleen, lung, kidney, and tumor of mice were collected at 0, 6, 12, 24, 36, and 48 h, respectively. Tissue samples were digested with concentrated aqueous HNO_3, and the amounts of Au and Ca were measured by inductively coupled plasma-mass spectrometry (ICP-MS). And the quantitative data were consistent with the fluorescence results; the highest Au and Ca accumulation in tumors was achieved at 24 h post injection of mPEG–PEI–AuNRs and mPEG–PEI/CaNPs (Figure S18, Supporting Information). The results indicated that the mPEG–PEI–AuNRs and mPEG–PEI/CaNPs could be gradually accumulated in the tumors, which could be mainly attributed to the enhanced permeability and retention effect of mPEG–PEI–AuNRs and mPEG–PEI/CaNPs.

Owing to the intrinsic property of the strong absorption in the NIR region, mPEG–PEI–AuNRs were potential PAI contrast agents. With the increasing Au concentrations from 0 to 25 μg mL^{-1}, PA signal intensity of mPEG–PEI–AuNRs dramatically increased, and the calculated PA signal values exhibited a linear relationship with the increasing concentrations of mPEG–PEI–AuNRs (Figure S19, Supporting Information). Next, PA signals of mPEG–PEI–AuNRs with or without mPEG–PEI/CaNPs were monitored at different pH conditions (**Figure 5**a; Figure S20, Supporting Information). As

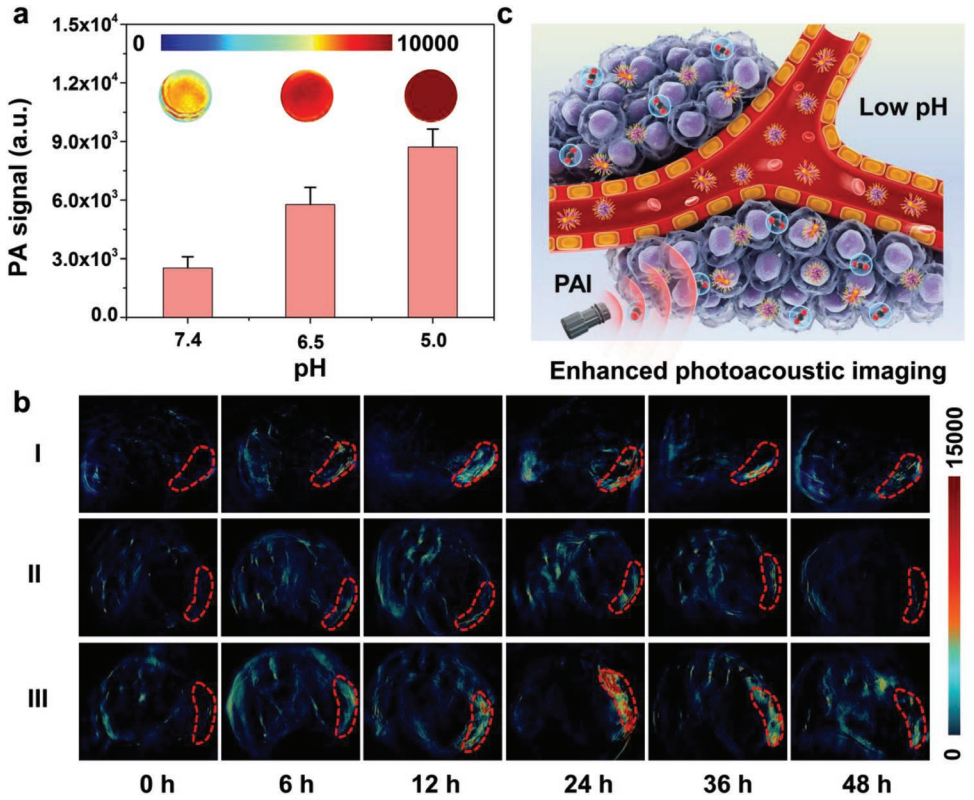

Figure 5. PAI evaluation in vitro and in vivo. a) PA signals of mPEG–PEI–AuNRs with mPEG–PEI/CaNPs at different pH conditions. The concentrations of the mPEG–PEI–AuNRs and mPEG–PEI/CaNPs were 2.5 and 10 μg mL^{-1}, respectively. b) The enhanced PA signals of mPEG–PEI–AuNRs with mPEG–PEI/CaNPs. I: mPEG–PEI–AuNRs, II: mPEG–PEI/CaNPs, III: mPEG–PEI–AuNRs + mPEG–PEI/CaNPs. c) The mechanism of enhancing PA signals with the generation of CO_2 bubbles in acidic pH in tumors.

shown in Figure 5a, PA signals of mPEG–PEI–AuNRs with mPEG–PEI/CaNPs were significantly enhanced at weakly acidic pH condition (pH 6.5). Notably, at pH 5.0, the PA signals of mPEG–PEI–AuNRs with mPEG–PEI/CaNPs reached the highest intensity, and the PA signals were more than three times higher than that of at pH 7.4. However, PA signals of mPEG–PEI–AuNRs without mPEG–PEI/CaNPs showed no significant change at different pH conditions (Figure S20, Supporting Information). These results indicated that the PA signals of mPEG–PEI–AuNRs could be effectively enhanced with the presence of mPEG–PEI/CaNPs, which was likely due to the generation of CO_2 bubbles in acidic pH condition. Furthermore, the enhanced PA signals of mPEG–PEI–AuNRs with mPEG–PEI/CaNPs were also detected at tumor tissue in vivo. As shown in Figure 5b, the signals at the tumor site were relatively low with mPEG–PEI/CaNPs or mPEG–PEI–AuNRs' injection alone, whereas the obvious PA signals were observed with mPEG–PEI/CaNPs and mPEG–PEI–AuNRs' injection together, which indicated that the PA signals of mPEG–PEI–AuNRs could be significantly enhanced with the presence of mPEG–PEI/CaNPs. The photoacoustic signals were quantified (Figure S21, Supporting Information), and the PA signals at the tumor site treated with mPEG–PEI–AuNRs and mPEG–PEI/CaNPs' injection together were significantly enhanced compared with mPEG–PEI–AuNRs or mPEG–PEI/CaNPs' injection alone. All these results indicated that the mPEG–PEI/CaNPs could generate CO_2 bubbles in acidic pH in tumors, which could be responsible for echogenic reflection under a US field (Figure 5c). The enhanced PA signals could be served as the contrast agents for guiding the precise tumor treatment.

2.6. In Vivo Antitumor Efficacy

Encouraged by the above-mentioned results, antitumor efficacy in vivo was evaluated by using MCF-7 tumor-bearing Balb/c nude mice. First, the photothermal heating profiles of tumors were monitored by an IR thermal camera (Figure S22, Supporting Information). After 24 h injection, the temperature of tumors on mice treated with mPEG–PEI–AuNRs rapidly increased to about 51 °C within 2 min under the laser irradiation, which was enough high to kill the tumor cells in vivo. However, the tumor temperature in the control group without mPEG–PEI–AuNRs' injection only showed slight increase to about 40 °C at the end of 6 min irradiation, which could not ablate tumors. The antitumor efficacy in vivo was conducted according to the relation shown in **Figure 6**a. The tumor volume was monitored as the function of time (Figure 6b). As shown in Figure 6b, the tumors in control group (PBS), PBS + Laser group, PBS + US irradiation group, mPEG–PEI/CaNPs group, mPEG–PEI–AuNRs group, and mPEG–PEI/CaNPs + mPEG–PEI–AuNRs group kept the natural growth trend, which indicated that mPEG–PEI/CaNPs and mPEG–PEI–AuNRs themselves could not effectively inhibit the tumor growth in the absence of US irradiation and NIR laser irradiation. However, the tumors in mice treated with mPEG–PEI/CaNPs were efficiently inhibited after the US irradiation. Moreover, the mPEG–PEI–AuNRs group showed apparent inhibition of tumor growth with NIR laser irradiation. Notably, it was found that the tumors in mice injected by mPEG–PEI/CaNPs and mPEG–PEI–AuNRs treated with US irradiation and NIR irradiation together were completely eliminated without recurrence during 24 days (Figure 6c). This was likely due to PTT and UST combination therapy. Under the NIR irradiation, the tumors could be ablated by the heat effect of mPEG–PEI–AuNRs. At the same time, the generation of CO_2 bubbles by mPEG–PEI/CaNPs at tumoral pH would instantly explode to destroy the tumor cells under US irradiation, and thus the tumors were inhibited (Figure 6d). Furthermore, no body weight change was observed in various groups (Figure S23, Supporting Information). In the treatment of mice, we changed the order of PTT and UST (Figure S24, Supporting Information). The mice were treated with PTT followed by UST, or first UST and then PTT. The results of tumor suppression are shown in Figure S24 (Supporting Information), and there was no difference in the results of tumor suppression, indicating that the order of treatment had no effect on the treatment results. Hematoxylin and eosin (H&E) staining images in combination with UST and PTT treatment group showed that no obvious damage of organs was displayed as compared to the organs from the control groups (Figure S25, Supporting Information). Also, the liver function (alanine aminotransferase, aspartate aminotransferase, and alkaline phosphatase; Figure S26, Supporting Information) and renal function parameters (creatinine, uric acid, and blood urea nitrogen; Figure S27, Supporting Information) in serum illustrated that there was no statistical significant difference between treated mice and control mice, indicating that mPEG–PEI/CaNPs and mPEG–PEI–AuNRs had low adverse effects in vivo. Therefore, the above results illustrated that the combination of UST and PTT could enhance the therapeutic efficiency with low side effects, strongly suggesting that mPEG–PEI/CaNPs and mPEG–PEI–AuNRs could serve as the candidate efficient agents for in vivo UST and PTT.

3. Conclusion

In summary, we successfully constructed two nanoparticles for enhanced PAI-guided PTT and UST. mPEG–PEI/CaNPs could generate CO_2 bubbles at tumoral pH. These CO_2 bubbles could not only enhance the PAI of mPEG–PEI–AuNRs, but also explode to mechanically destroy tumor cells under ultrasonic irradiation. Moreover, significant tumor ablation was achieved after intravenous administration of mPEG–PEI–AuNRs with NIR laser irradiation. Most importantly, mPEG–PEI–AuNRs and mPEG–PEI/CaNPs together could achieve effective eradication of tumors under combined PTT and UST. Therefore, mPEG–PEI–AuNRs and mPEG–PEI/CaNPs could hold great potential for accurate cancer diagnosis to guide the NIR laser and US irradiation for efficient inhibition of tumors with low side effects. The approach might provide a valuable direction for simultaneous cancer diagnostics and therapeutics.

4. Experimental Section

Materials: Branched polyethylenimine with a molecular weight of 25 000 Da (PEI25k) was purchased from Sigma–Aldrich (Saint Louis, MO, USA). Tetrachloroauric acid ($HAuCl_4{\cdot}4H_2O$) was obtained from

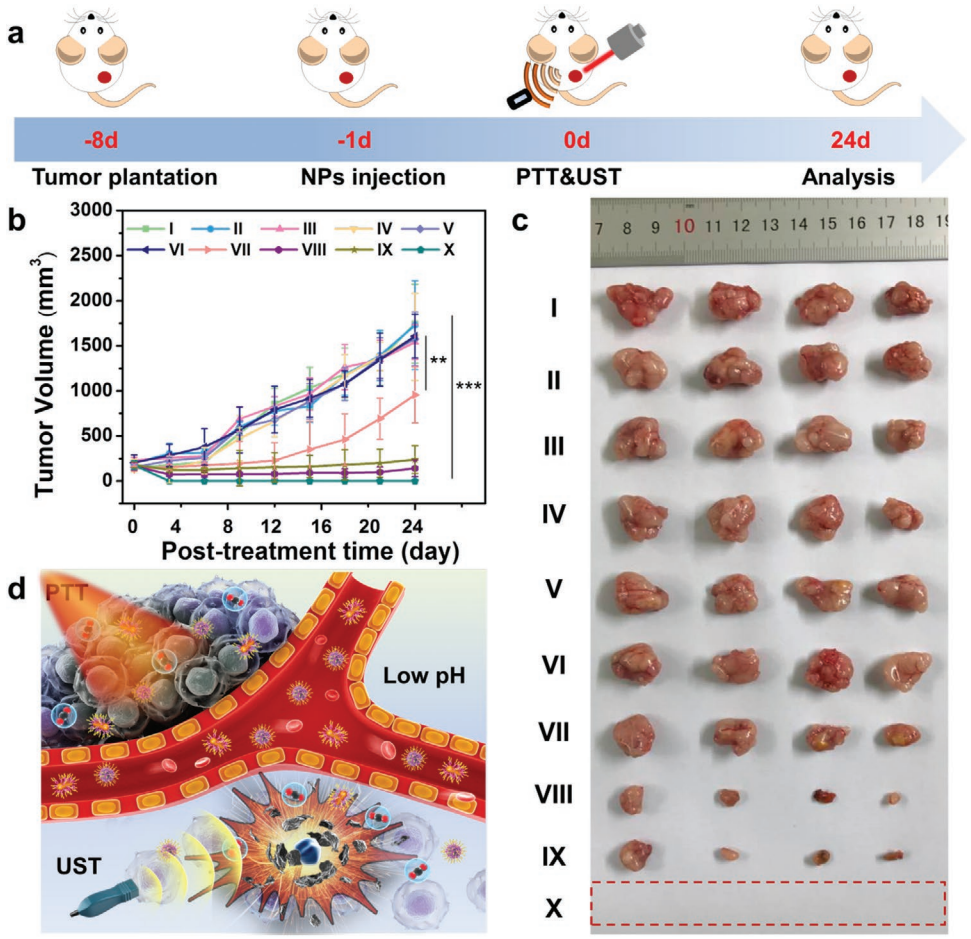

Figure 6. In vivo antitumor efficacy. a) Schematic illustration of the combination with PTT and UST to inhibit tumor growth in the MCF-7 tumor-bearing Balb/c nude mice model. b) Time-dependent tumor growth curves of the mice after different treatments. c) Representative photos of tumors 24 days after treatments. I: PBS, II: PBS + Laser, III: PBS + US irradiation, IV: mPEG–PEI/CaNPs, V: mPEG–PEI–AuNRs, VI: mPEG–PEI/CaNPs + mPEG–PEI–AuNRs, VII: mPEG–PEI/CaNPs + US irradiation, VIII: mPEG–PEI–AuNRs + Laser, IX: mPEG–PEI/CaNPs + mPEG–PEI–AuNRs + Laser, X: mPEG–PEI/CaNPs + mPEG–PEI–AuNRs + Laser + US irradiation. d) Schematic diagram of the combination with PTT and UST of mPEG–PEI/CaNPs and mPEG–PEI–AuNRs.

Shanghai Chemical Reagent Co., Ltd. (Shanghai, China). Methoxy poly(ethylene glycol) with a molecular weight of 5000 Da was purchased from Sigma–Aldrich (Saint Louis, MO, USA). $CaCl_2{\cdot}2H_2O$ and NH_4HCO_3 were purchased from Aladdin (Shanghai, China). Cy5 *N*-hydroxysuccinimide (NHS) ester was obtained from Lumiprobe Corporation (Broward, FL, USA). Dulbecco's modified Eagle's medium (DMEM) was purchased from Gibco (Grand Island, NY, USA). All other chemicals and materials were obtained from Sigma–Aldrich (Saint Louis, MO, USA) unless otherwise mentioned.

Characterizations: TEM images were obtained on a JEOL JEM-1011 transmission electron microscope (Tokyo, Japan) operated at 100 kV. The FTIR spectra were acquired with a Bio-Rad Win-IR instrument (Bio-Rad Laboratories Inc., Cambridge, MA, USA). The UV–vis–NIR absorption spectra were recorded by an ultraviolet–visible (UV–vis) spectro-photometer (2401PC, Varian) at room temperature. The Au and Ca elemental analyses were performed on an ELAN 9000/DRC ICP-MS system (PerkinElmer, USA).

Synthesis of mPEG–PEI–AuNRs: The AuNRs were prepared using a seed-mediated growth method, and PEI was modified on the surface of AuNRs via the sulfur–gold bond.[16,22] In brief, 0.08 g of NHS (98.0%), 0.08 g of 1-ethyl-3-(3-dimethylaminopropyl) carbodi-imide hydrochloride (EDC·HCl, 98.5%), and 0.8 g of PEI in aqueous solution (15 mL) were added to 0.04 g of mercaptopropionic acid in aqueous solution (10 mL). After 24 h of reaction at 30 °C, 0.02 g of as-prepared AuNRs was added to PEI−SH solution for another 24 h at 30 °C. PEI–AuNRs were separated via centrifugation at 6000 rpm for 10 min to remove the unreacted reagents, and the precipitate was washed with deionized water twice. Finally, the precipitate was redispersed in deionized water and the PEI–AuNRs were prepared successfully.

The mPEG−CHO was synthesized and purified as previously described.[17,20] mPEG–PEI–AuNRs or mPEG–PEI were prepared by adding mPEG–CHO aqueous solution into PEI–AuNRs or PEI at 5:1 mass ratio (mPEG–CHO:PEI) at pH 8.0 and incubated at room temperature for 2 h. And mPEG–PEI was detected by ^{1}H NMR with a Bruker AV-300 NMR spectrometer.

Preparation of mPEG–PEI/CaNPs: $CaCl_2{\cdot}2H_2O$ (200 mg) was dissolved in ethanol (100 mL) and placed in a beaker, then covered by parafilm with several small pores and put it in a desiccator at 30 °C. Two beakers of NH_4HCO_3 were left in the same desiccator. After vapor diffusion reaction for 3 days, the products were centrifuged and redispersed in 1% sodium dodecyl sulfate (SDS) aqueous solution. The solution was centrifuged at 8000 rpm and washed with deionized water twice. Finally, CaNPs were prepared and sonicated in deionized water for 20 min for later use. As-prepared mPEG–PEI in aqueous solution was added into CaNPs at a 1:1 mass ratio (PEI:Ca), and the mPEG–PEI/CaNPs were prepared via electrostatic interaction.

Labeling Cy5 of mPEG–PEI–AuNRs and mPEG–PEI/CaNPs: 25 µL of Cy5 NHS (1 mg mL^{-1}) was respectively added to the 1 mL mPEI–AuNRs (Au, 200 µg mL^{-1}), mPEG–PEI–AuNRs (Au, 200 µg mL^{-1}), PEI/CaNPs (Ca, 100 µg mL^{-1}), and mPEG–PEI/CaNPs (Ca, 100 µg mL^{-1}) with stirring for overnight; the labeled PEI–AuNRs, mPEG–PEI–AuNRs, PEI/CaNPs, and mPEG–PEI/CaNPs were performed three centrifugation/redispersion cycles to remove the excess free Cy5.

Intracellular Uptake: The intracellular uptake of mPEG–PEI–AuNRs and mPEG–PEI/CaNPs was carried out by FCM and CLSM. For cytometric analysis, MCF-7 cells were seeded in 12-well plates at a density of 1.0×10^5 cells per well for 24 h. The medium was changed by fresh medium at pH 7.4 and 6.5, then Cy5-labeled PEI–AuNRs, mPEG–PEI–AuNRs, PEI/CaNPs, and mPEG–PEI/CaNPs were added to each well. After 3 h of incubation, the cells were detached and resuspended with cold PBS. Finally, the cells were monitored using a Guava EasyCyte flow cytometer (Merck Millipore, Billerica, MA, USA). For the CLSM studies, MCF-7 cells were seeded in 6-well plates at a density of 1.0×10^5 cells per well for 24 h. The medium was placed by fresh medium of pH 7.4 and 6.5, then Cy5-labeled PEI–AuNRs, mPEG–PEI–AuNRs, PEI/CaNPs, and mPEG–PEI/CaNPs were added to each well for 3 h. The cells were washed by PBS and dyed with 4'-6-diamidino-2-phenylindole (DAPI, 1 mg mL^{-1}, 1 µL per well) for 5 min. After washing by PBS, the cells were observed using by CLSM (ZEISS LSM 780, Oberkochen, Germany).

In Vitro Photothermal Performance of mPEG–PEI–AuNRs: To evaluate photothermal performance of mPEG–PEI–AuNRs, 200 µL of mPEG–PEI–AuNRs aqueous solutions at different Au concentrations was continuously irradiated with an 808 nm laser at 0.8 W cm^{-2} for 10 min. The temperature during the process was recorded by the infrared imaging camera (FLIR E5; FLIR System AB, Täby, Sweden). Deionized water was set as the control. The mPEG–PEI–AuNRs' aqueous solution was exposed to 808 nm laser for 10 min, and cooled into room temperature for four cycle to evaluate the photostability. The photothermal conversion efficiency (η) of mPEG–PEI–AuNRs was calculated according to the previous methods.[23]

In Vitro Photothermal Therapy and Ultrasonic Therapy: mPEG–PEI–AuNRs and mPEG–PEI/CaNPs at different concentrations were incubated alone or in combination with MCF-7 or HeLa cells. For PTT, cells were subjected to 808 nm laser at 0.8 W cm^{-2} for 6 min. For UST, the cells were radiated for 10 min at 1 Hz, 1.5 W cm^{-2} on a portable ultrasonic therapy device (838A-H-O-S, SX Ultrasonic, Shenzhen, China). The cells were incubated for further 24 h and washed with cold PBS twice. Subsequently, the cell viability was detected by the MTT method at 492 nm with a Bio-Rad 680 Microplate Reader. For further confirming in vitro PTT and UST, MCF-7 or HeLa cells were placed in a 24-well plate (8×10^4 cells per well). After overnight incubation, mPEG–PEI–AuNRs and mPEG–PEI/CaNPs at different concentrations were added alone or in combination into cells. Then cells were treated with 808 nm laser at 0.8 W cm^{-2} for 6 min or portable ultrasonic therapeutic apparatus at 1 Hz, 1.5 W cm^{-2} for 10 min, and incubated for another 20 h. Finally, cells were stained with Calcein AM and PI, and observed using a fluorescence microscope (Tokyo, Japan).

In Vivo Fluorescence Imaging: All animal studies were performed with guidelines for laboratory animals established by Jilin University. MCF-7 tumor-bearing Balb/c nude mice were injected via tail vein with Cy5-labeled mPEG–PEI–AuNRs (Au, 200 µg mL^{-1}) and mPEG–PEI/CaNPs (Ca, 100 µg mL^{-1}), respectively. The heart, liver, spleen, lung, kidney, and tumor of mice were excised at 6, 12, 24, 36, and 48 h post administration. The fluorescence distribution in tissues was captured by a Maestro in vivo Imaging System (Cambridge Research & Instrumentation Inc., USA).

Enhanced PAI: A phantom composed of agarose gel was used for PA signal detection in vitro. Various concentrations of mPEG–PEI–AuNRs and mPEG–PEI/CaNPs at pH 7.4, 6.5, and 5.0 were placed into wells of phantom gel. PAI was performed with a commercial MSOT InVision128 PA tomography system (iThera Medical, Germany). For enhancing PAI signals in vivo, mPEG–PEI–AuNRs and mPEG–PEI/CaNPs were injected into mice via tail vein, the PA signals of tumor at different time points were collected with multispectral process scanning.

In Vivo PTT and UST: The MCF-7 tumor-bearing mice were randomly divided into ten groups. The mPEG–PEI–AuNRs and mPEG–PEI/CaNPs were injected alone or in combination via tail vein. PBS was set as control. After 24 h injection, PTT and UST were performed by irradiating the tumor regions with an 808 nm laser at 1.0 W cm^{-2} for 6 min and portable ultrasonic therapeutic apparatus at 1 Hz, 1.5 W cm^{-2} for 10 min. For the PTT alone group, the infrared thermal images were recorded at different irradiation times. Tumor sizes were measured every other day for the maximum length (A) and width (B), and the tumor volumes (V) were calculated as the formula: $V = (AB^2)/2$. H&E staining was performed and observed by a bright-field microscope (Tokyo, Japan). The levels of liver function markers and kidney function markers were determined by enzyme-linked immunosorbent assay (ELISA, Lengton Bio, Shanghai, China).

Statistical Analysis: Values were expressed as the mean ± standard deviations (SD). Statistical analysis was performed by two-sided Student's t-test for two groups using GraphPad Prism (GraphPad Software Inc., CA, USA). Probabilities values as $p < 0.05$ (*), $p < 0.01$ (**), and $p < 0.001$ (***) were considered statistically significant.

Supporting Information

Supporting Information is available from the Wiley Online Library or from the author.

Acknowledgements

The authors are thankful to National Natural Science Foundation of China (Grant Nos. 52073278, 51925305, 51873208, 51520105004, 51833010, 51803210, and 51973217), National Science and Technology Major Projects for Major New Drugs Innovation and Development (Grant No. 2018ZX09711003-012), National Program for Support of Top-Notch Young Professionals, Jilin Province Science and Technology Development program (20180414027GH).

Conflict of Interest

The authors declare no conflict of interest.

Keywords

calcium carbonate nanoparticles, CO_2 bubbles, combining photothermal therapy with ultrasonic therapy, enhancing photoacoustic imaging, gold nanorods

Received: October 31, 2020
Published online:

[1] a) M. Xu, L. V. Wang, *Rev. Sci. Instrum.* **2006**, *77*, 041101; b) L. V. Wang, S. Hu, *Science* **2012**, *335*, 1458.
[2] a) A. Hannah, G. Luke, K. Wilson, K. Homan, S. Emelianov, *ACS Nano* **2014**, *8*, 250; b) J. C. Li, K. Y. Pu, *Chem. Soc. Rev.* **2019**, *48*, 38.
[3] Y. Liu, P. Bhattarai, Z. Dai, X. Chen, *Chem. Soc. Rev.* **2019**, *48*, 2053.
[4] X. Liang, Z. Deng, L. Jing, X. Li, Z. Dai, C. Li, M. Huang, *Chem. Commun.* **2013**, *49*, 11029.
[5] M. Eghtedari, A. Oraevsky, J. A. Copland, N. A. Kotov, A. Conjusteau, M. Motamedi, *Nano Lett.* **2007**, *7*, 1914.
[6] K. Wilson, K. Homan, S. Emelianov, *Nat. Commun.* **2012**, *3*, 618.
[7] K. Ferrara, R. Pollard, M. Borden, *Annu. Rev. Biomed. Eng.* **2007**, *9*, 415.

[8] S. Qin, C. F. Caskey, K. W. Ferrara, *Phys. Med. Biol.* **2009**, *54*, R27.
[9] K. Zhang, H. Xu, H. Chen, X. Jia, S. Zheng, X. Cai, R. Wang, J. Mou, Y. Zheng, J. Shi, *Theranostics* **2015**, *5*, 1291.
[10] a) M. Chung, K. Chen, H. Liang, Z. Liao, W. Chia, Y. Xia, H. Sung, *Angew. Chem., Int. Ed.* **2012**, *51*, 10089; b) E. G. Schutt, D. H. Klein, R. M. Mattrey, J. G. Riess, *Angew. Chem., Int. Ed.* **2003**, *42*, 3218.
[11] K. H. Min, H. S. Min, H. J. Lee, D. J. Park, J. Y. Yhee, K. Kim, I. C. Kwon, S. Y. Jeong, O. F. Silvestre, X. Chen, Y.-S. Hwang, E.-C. Kim, S. C. Lee, *ACS Nano* **2015**, *9*, 134.
[12] a) J. Nam, S. Son, L. J. Ochyl, R. Kuai, A. Schwendeman, J. J. Moon, *Nat. Commun.* **2018**, *9*, 1074; b) Q. Chen, L. Xu, C. Liang, C. Wang, R. Peng, Z. Liu, *Nat. Commun.* **2016**, *7*, 13193; c) Y. Y. Jiang, D. Cui, Y. Fang, X. Zhen, P. K. Upputuri, M. Pramanik, D. Ding, K. Y. Pu, *Biomaterials* **2017**, *145*, 168.
[13] a) J. Chen, C. Ning, Z. Zhou, P. Yu, Y. Zhu, G. Tan, C. Mao, *Prog. Mater. Sci.* **2019**, *99*, 1; b) H. S. Jung, P. Verwilst, A. Sharma, J. Shin, J. L. Sessler, J. S. Kim, *Chem. Soc. Rev.* **2018**, *47*, 2280; c) C. Xu, Y. Wang, H. Yu, H. Tian, X. Chen, *ACS Nano* **2018**, *12*, 8255; d) Y. Wang, Z. Wang, C. Xu, H. Tian, X. Chen, *Biomaterials* **2019**, *197*, 284; e) J. C. Li, D. Cui, J. G. Huang, S. S. He, Z. B. Yang, Y. Zhang, Y. Luo, K. Y. Pu, *Angew. Chem., Int. Ed.* **2019**, *58*, 12680; f) J. C. Li, J. G. Huang, Y. Lyu, J. S. Huang, Y. Y. Jiang, C. Xie, K. Y. Pu, *J. Am. Chem. Soc.* **2019**, *141*, 4073; g) X. Zhen, C. Xie, Y. Jiang, X. Ai, B. Xing, K. Pu, *Nano Lett.* **2018**, *18*, 1498.
[14] a) Y. Z. Wang, Y. J. Song, G. X. Zhu, D. C. Zhang, X. W. Liu, *Chin. Chem. Lett.* **2018**, *29*, 1685; b) S. Liu, L. Wang, M. Lin, Y. Liu, L. Zhang, H. Zhang, *Chin. J. Polym. Sci.* **2019**, *37*, 115.
[15] a) C. Tran, J. Seo, T. L. Hall, J. B. Fowlkes, C. A. Cain, *IEEE Trans. Ultrason. Ferroelectr. Freq. Control* **2003**, *50*, 1296; b) X. Q. Lu, E. C. Burdette, B. A. Bornstein, J. L. Hansen, G. K. Svensson, *Int. J. Hyperthermia* **1996**, *12*, 375.
[16] J. Chen, H. Liang, L. Lin, Z. Guo, P. Sun, M. Chen, H. Tian, M. Deng, X. Chen, *ACS Appl. Mater. Interfaces* **2016**, *8*, 31558.
[17] X. Guan, Z. Guo, L. Lin, J. Chen, H. Tian, X. Chen, *Nano Lett.* **2016**, *16*, 6823.
[18] N. Yan, X. Wang, L. Lin, T. Song, P. Sun, H. Tian, H. Liang, X. Chen, *Adv. Funct. Mater.* **2018**, *28*, 1800490.
[19] J. Casas, M. Venkataramasubramani, Y. Wang, L. Tang, *Biosens. Bioelectron.* **2013**, *49*, 525.
[20] X. Guan, Z. Guo, T. Wang, L. Lin, J. Chen, H. Tian, X. Chen, *Biomacromolecules* **2017**, *18*, 1342.
[21] M. Hessel, V. P. Pattani, M. Rasch, M. G. Panthani, B. Koo, J. W. Tunnell, B. A. Korgel, *Nano Lett.* **2011**, *11*, 2560.
[22] B. Nikoobakht, M. A. El-Sayed, *Chem. Mater.* **2003**, *15*, 1957.
[23] M. Chu, W. Hai, Z. Zhang, F. Wo, Q. Wu, Z. Zhang, Y. Shao, D. Zhang, L. Jin, D. Shi, *Biomaterials* **2016**, *91*, 182.